//:... GRANT
/N-02-CR
//5/30
P. /7

Final Report: Year 2

Nonlinear Aerodynamics and the Design of Wing Tips

Conducted for the
National Aeronautics and Space Administration
Ames Research Center
Grant # NCC2-683

Covering the Period
1 April 1991 to 31 March 1992

by the
Department of Aeronautics and Astronautics
Stanford, California 94305

Principal Investigator
Ilan Kroo

Research Assistant
Sean Wakayama

April 1992

CASI

Introduction

This contract began in April 1990 with studies on the effect of wingtip shape on induced drag. That work considered problems of determining induced drag from computational aerodynamic methods and examined effects of wake roll up on the induced drag of elliptical and crescent wings, [1].

The research contract was continued in April 1991 with scope augmented to include considerations other than induced drag. The idea was to develop methods for comparing wing tip shapes on the basis of their effects on total drag, structural weight, and high lift performance. To accomplish this, work was done to improve methods for multidisciplinary analysis and optimization of wings.

This report describes results of research conducted from April 1991 through March 1992. The general objective was to improve an existing wing optimization method, [2], and apply the method to specific problems of interest. The method, while a valuable tool for wing tip design studies, can be applied to more general problems, and has been applied to some of these other problems during its development.

Specific goals that were accomplished are listed below and are explained in more detail in the report.

1. Improvements were made to the portability and control flow of the existing code. The major iteration loop dealing with structural design was sped up and an alternate approach, using the optimizer to do structural sizing, was studied.

2. Analysis methods were improved in the areas of structural and high lift modelling. The structural method was revised to give total wing weight and verified against data for particular commercial aircraft. The high lift analysis was improved to provide reasonable estimates of C_{Lmax} in the flaps down condition. These improvements enabled making wing area a design variable, where it had been a fixed variable in the original method.

3. The method was applied to the design of wings for a Learjet. Rough studies were done to determine the effects of laminar flow design on wing shape.

4. Studies on wingtip shape were begun.

Nomenclature

Structural Sizing:

α	Step length parameter.
$\{t_s\}$	Skin thickness.
$\{t_{sFS}\}$	Minimum skin thickness constraint.
$\{t_{serr}\}$	Difference between actual and minimum skin thickness.

Wing Analysis:

c	Chord.
c_h, c_{xx}, c_{hh}	Constants for induced flap deflection fit.
C_L	Configuration lift coefficient.
C_{Lmax}	Maximum configuration lift coefficient.
c_l	Section lift coefficient.
c_{lmax}	Maximum allowable section lift coefficient.
Δc_l	Increment to section lift due to flap deflection at zero angle of attack.
Δc_{lmax}	Increment to maximum allowable section lift coefficient due to flap deflection.
$c_{l\alpha}$	Lift curve slope.
$c_{l\delta}$	Flap lift curve slope.
E	Young's modulus.
G	Shear modulus.
h	Distance between points in y-z plane.
$\hat{n}$	Local panel unit normal vector.
t	Wing thickness.
t/c	Thickness to chord ratio.
U_∞	Freestream velocity.
v	Velocity.
x	Coordinate direction, nominally along freestream.
y	Coordinate direction, nominally pointing to aircraft right.
z	Coordinate direction, nominally pointing up.
α	Angle of attack.
δ	Flap deflection.
δ_g	Geometric flap deflection.
δ_i	Flap deflection due to induced velocities.
Γ	Vortex strength.
Λ	Wing sweep.
σ_y	Yield stress.
$\hat{\theta}$	Unit normal vector in direction of velocity induced by shed vorticity at flap edge.

Improvements to Code

Portability

The code was made more portable. It runs in interactive mode on the Macintosh computer and in batch mode on many workstations and mainframe computers, including Sun, Iris, DEC, and Cray Y-MP platforms.

Structural Sizing Algorithm

A fast algorithm was developed for sizing skin thicknesses. This task is an iterative process because of aeroelasticity: changing the skin thicknesses to meet stress constraints changes the elasticity of the wing, which in turn affects the loads and stresses. The developed algorithm attempts to determine, in the least amount of time, the skin thicknesses that meet maximum stress and minimum gauge constraints.

Each iteration in the algorithm begins with an initial guess of the skin thickness, $\{t_s\}_1$. Structural loads are calculated using this guess, and a new set of thicknesses are found that meet the stress constraints under those loads, $\{t_{s_{FS}}\}$. The difference between $\{t_{s_{FS}}\}_1$ and $\{t_s\}_1$ is the skin thickness error.

$$\{t_{s_{err}}\}_1 = \{t_{s_{FS}}\}_1 - \{t_s\}_1$$

Perturbations that are proportional to the error distribution are considered about the initial guess.

$$\{t_s\} = \{t_s\}_1 + \alpha \, \{t_{s_{err}}\}_1$$

The error distribution is approximated as varying linearly with the step length, α.

$$\{t_{s_{err}}\} = \{t_{s_{err}}\}_1 + \alpha \, \left\{\frac{dt_{s_{err}}}{d\alpha}\right\}$$

The change in error relative to step length, $\left\{\frac{dt_{s_{err}}}{d\alpha}\right\}$, can be estimated using finite differences. The step length minimizing the mean square error is used to determine the next guess of the skin thickness. The mean square error can be written as follows.

$$\{t_{s_{err}}\} \cdot \{t_{s_{err}}\} = \{t_{s_{err}}\}_1 \cdot \{t_{s_{err}}\}_1 +$$
$$2\alpha\{t_{s_{err}}\}_1 \cdot \left\{\frac{dt_{s_{err}}}{d\alpha}\right\} + \alpha^2 \left\{\frac{dt_{s_{err}}}{d\alpha}\right\} \cdot \left\{\frac{dt_{s_{err}}}{d\alpha}\right\}$$

Minimizing with respect to α yields

$$\alpha = -\frac{\{t_{s_{err}}\}_1 \cdot \left\{\frac{dt_{s_{err}}}{d\alpha}\right\}}{\left\{\frac{dt_{s_{err}}}{d\alpha}\right\} \cdot \left\{\frac{dt_{s_{err}}}{d\alpha}\right\}}$$

The iteration steps are summarized below.

1. Using the current guess of the skin thickness distribution, $\{t_s\}_1$, calculate loads under all structural design conditions. Flag the critical conditions that violate the maximum stress constraint. For the calculated loads, determine the skin thicknesses that meet the stress constraint, $\{t_{s_{FS}}\}_1$, and the skin thickness error, $\{t_{s_{err}}\}_1$.

2. Using $\{t_s\}_2 = \{t_{s_{FS}}\}_1$ for the skin thickness distribution, calculate loads under the critical conditions found in step 1. Determine skin thicknesses to meet the stress constraint, $\{t_{s_{FS}}\}_2$, and the skin thickness error, $\{t_{s_{err}}\}_2 = \{t_{s_{FS}}\}_2 - \{t_s\}_2$.

3. Calculate the change in skin thickness error. Since $\alpha = 1$ in step 2, $\left\{\frac{dt_{s_{err}}}{d\alpha}\right\} = \{t_{s_{err}}\}_2 - \{t_{s_{err}}\}_1$. Estimate the step length, α.

$$\alpha = -\frac{\{t_{s_{err}}\}_1 \cdot \left\{\frac{dt_{s_{err}}}{d\alpha}\right\}}{\left\{\frac{dt_{s_{err}}}{d\alpha}\right\} \cdot \left\{\frac{dt_{s_{err}}}{d\alpha}\right\}}$$

Evaluate the next guess for skin thickness.

$$\{t_s\} = \{t_s\}_1 + \alpha \, \{t_{s_{err}}\}_1$$

The algorithm loops from step 3 to step 1 and terminates when $\{t_{s_{err}}\}_1$ is sufficiently small. Neglecting non-critical conditions in step 2 saves time by avoiding load cases that do not affect the required skin thicknesses. The calculation of α is protected against division by zero errors and is prevented from excessively large values.

Optimizer Directed Structural Sizing

Using the optimizer to handle skin thicknesses as design variables was examined as an alternate way to do structural sizing. This has potential advantages over the structural sizing algorithm described above. Optimizer directed structural sizing eliminates the internal iteration on skin thicknesses, leading to a simplified program structure, figures 1 and 2. It could also reduce overall optimization time by reducing the cost of a function evaluation and eliminating function noise due to the internal iteration loop. The potential disadvantage is increased optimization time due to the addition of design variables for the skin thicknesses.

To compare optimizer directed structural sizing against internal iterative sizing, the two methods were run on the same problem. The primary task was to optimize wing shape for minimum drag subject to fixed weight, low speed lift, and low speed handling constraints. The specific design variables and constraints are listed in tables 1 and 2.

Design variables and constraints relating to the primary task were handled identically in the runs of both methods. This eliminated differences in scaling and step size as a factor affecting optimization efficiency. For auxiliary design variables and constraints associated with the skin thickness sizing task, scaling and step size were selected to give fast convergence to a reasonable answer.

From table 1 and the drawing in figure 3, the two methods appear to have found the same answer. Table 2 indicates that constraints are closely met. The final value of the objective function from the two methods is close but not exact. This is partially due to the linearly varying skin thickness approximation used in the optimizer controlled method. While the internal iteration
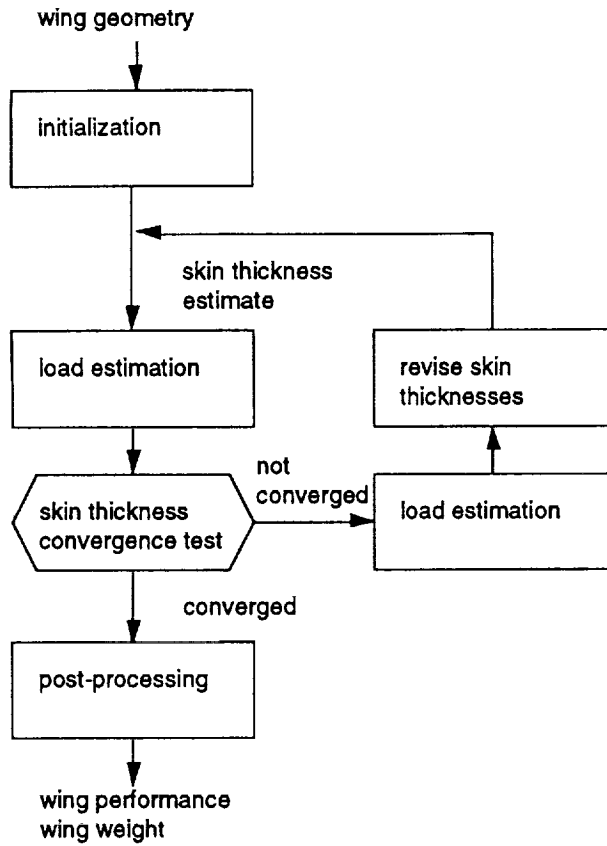
2

wing geometry

initialization

skin thickness estimate

load estimation → revise skin thicknesses

skin thickness convergence test — not converged → load estimation

converged

post-processing

wing performance
wing weight

Figure 1: Program Structure for Iterative Skin Thickness Sizing.

wing geometry
skin thicknesses

initialization

load estimation

post-processing

wing performance
wing weight
skin thickness error

Figure 2: Program Structure for Optimizer Directed Skin Thickness Sizing.
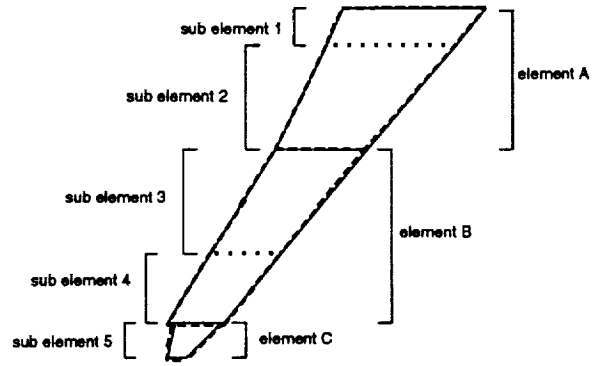

Figure 3: Optimized Wing Planforms and Element Layout. The planform found with skin thicknesses calculated by the optimizer, thin solid, is overlaid on the planform found with the internal iterative solution, heavy dashed. The layout of elements and sub elements is indicated to clarify the description in tables 1 and 2.

method determines the fully stressed skin thickness at each panel, the optimizer directed method does this for select stations on the wing. Shown in figure 4, this results in some extra material in the wing that is not required for stress or minimum gauge criteria. This disadvantage causes the resulting objective function from the optimizer controlled approach to be slightly larger than the result using internal iteration.

Details of the two optimizations are shown in table 3. Using the optimizer in place of an internal iteration requires more function evaluations, mainly because the increased number of design variables requires additional function evaluations for gradient calculations.

The optimizer controlled method used fewer optimization iterations, but this difference is mainly a matter of how long the optimizer took to decide that it could not improve the objective function. Shown in the iteration histories, figure 5, the two methods converge to their respective optimums in a similar manner. As explained earlier, the final objective function values are slightly different because the skin thickness distribution from the optimizer directed solution is more coarse than that from the internal iteration.

In a practical sense, both optimization runs arrived at their optimums with the same number of iterations. The iterations beyond number 40 were taken to exhaust the optimizer's ability to improve the objective function. This process consumes an unreliable number of iterations; variations in this number can be large. This makes the 25% overall time savings of the optimizer directed method not very meaningful. The time per iteration is meaningful, however, because it compares

3

Design Variable	Scale	Finite Difference Step	Internal Iteration Result	Optimizer Directed Result
BaseSemiSpan	1.0	1.0e-2	14.0	13.9
AreaFracA	50.	1.0e-4	0.535	0.534
AreaFracC	100.	1.0e-4	3.90e-2	3.89e-2
TaperA	10.	5.0e-4	0.643	0.646
TaperC	10.	5.0e-4	0.459	0.459
SweepA	0.1	.02	37.1	36.9
IncR1	0.1	.02	1.31	1.43
IncT2	0.1	.02	0.02	0.11
IncT4	0.1	.02	-3.22	-3.28
IncR5	0.1	.02	-3.03	-3.04
IncT5	0.1	.02	-4.06	-4.04
TonCR1	10.	1.0e-3	0.136	0.135
TonCT2	10.	1.0e-3	0.117	0.117
TonCT4	10.	1.0e-3	0.125	0.124
TonCR5	10.	1.0e-3	0.122	0.122
TonCT5	10.	1.0e-3	0.125	0.124
TsR1	.01	1.0e-3		12.6
TsR2	.01	1.0e-3		12.0
TsR3	.01	1.0e-3		9.8
TsR4	.01	1.0e-3		2.5
TsR5	.01	1.0e-3		1.0
TsT1	.01	1.0e-3		11.9
TsT2	.01	1.0e-3		9.8
TsT3	.01	1.0e-3		2.6
TsT4	.01	1.0e-3		0.8
TsT5	.01	1.0e-3		1.0

Table 1: Design Variables. Design variables used are shown with respective scaling factors, finite difference step sizes, and results from the two optimization methods. BaseSemiSpan is the wing semi span. AreaFracA and AreaFracC are the fractions of total wing semi area allocated to elements A and C respectively. (Elements and sub elements are marked in figure 3.) TaperA and TaperC are taper ratios of the elements. AreaFracB and TaperB are determined from a fixed area constraint and continuity of chord between elements A and B. SweepA is the wing quarter chord sweep. Inc, TonC, and Ts are, respectively, incidence, thickness to chord ratio, and skin thickness values for the sub elements. Location on the sub element is given by the suffixed R or T: R for root, T for tip. Final digit suffix indicates which sub element. Values not given in the table are defined by linearly interpolating between given values. The distributions are continuous unless multiple values are presented for the same location. For example, while IncT4 and IncT5 represent incidences for adjacent points on the wing, their values are different indicating a discontinuity.

Constraint	Scale	Limiting Value (type)	Internal Iteration Result	Optimizer Directed Result
Weight	.001	1405.05 (e)	1405.05	1405.05
CRollHL	100.	-0.02434 (u)	-0.02434	-0.02434
TsErrR1	1.0	0.0 (l)		-1.5e-5
TsErrR2	1.0	0.0 (l)		-1.4e-5
TsErrR3	1.0	0.0 (l)		-2.1e-5
TsErrR4	1.0	0.0 (l)		-5.1e-6
TsErrR5	1.0	0.0 (l)		0.0
TsErrT1	1.0	0.0 (l)		-1.4e-5
TsErrT2	1.0	0.0 (l)		-2.1e-5
TsErrT3	1.0	0.0 (l)		-5.6e-6
TsErrT4	1.0	0.0 (l)		-4.3e-14
TsErrT5	1.0	0.0 (l)		0.0

Table 2: Constraints. Constraints are shown with respective scaling factors, limiting values, and results from the two optimization methods. The type markings for the limiting values, shown in parentheses, indicate whether the limiting value was an equality constraint (e), an upper bound (u), or a lower bound (l). Weight is an index indicating the amount of bending material needed in the wing. CRollHL is an estimate of maximum rolling moment coefficient due to aileron deflection at low speed. TsErrR and TsErrT are the difference between actual skin thickness and minimum constraints at sub element root and tip panels respectively. The suffixing digit indicates the affected sub element. (Refer to figure 3 for sub element locations.)

Property	Internal Iteration Result	Optimizer Directed Result
Objective Function Value	.03484	.03496
Function Evaluations	2362	3237
Optimization Iterations	63	55
CPU Time (Cray Y-MP seconds)	482	360

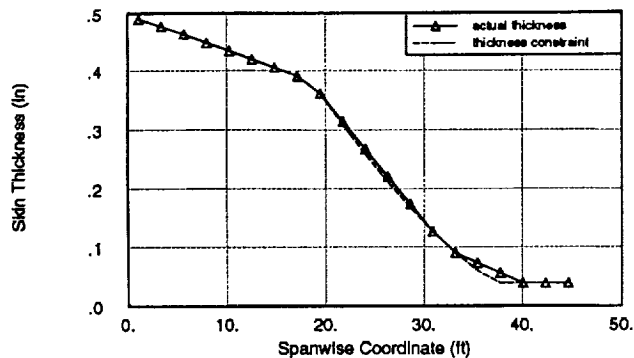Table 3: Optimization Details.

Figure 4: Skin Thickness Distributions. Skin thicknesses sized by the optimizer are shown against minimal skin thicknesses required to meet stress and minimum gauge requirements. Note that the structure is virtually fully stressed, with deviations due only to the linear approximation of skin thickness between break points. These deviations cause the structure to be slightly less efficient than the structure estimated by the internal solution method, and causes a small difference in optimal objective function value between the two solutions.

Figure 5: Iteration Histories. Both internal iteration and optimizer directed results are shown. The difference in final objective function value is due to differences in representation of the skin thickness distribution. (See figure 4.)

the cost of many simple function evaluations with the cost of fewer evaluations possessing internal iterations. In this respect, the optimizer directed method was still better, taking 14% less time per optimization iteration than the internal iteration method.

Since the optimizer directed solution uses 57% more function evaluations per optimizer iteration, it can be inferred that each function evaluation takes 55% less time than a function evaluation with internal iteration. This suggests that the per function evaluation time savings from removing an internal iteration loop must be large for the optimizer directed method to be effective, especially if removing the loop will greatly increase the number of design variables.

This study showed that it can be advantageous to use optimization for controlling analyses requiring iterative solution. While simplifying the coding needed for the analysis, optimizer directed iteration can reduce computational time when the cost of internal iteration is large and the number of extra design variables associated with replacing the iteration is small.

Analysis Improvements

Structural Design

Improvements in structural design were aimed at accurately predicting wing weight and static aeroelastic deformations. The resulting model with its verification studies are described below.

The wing structural model includes only the box section between front and rear spars. All load is assumed to be carried in the structural box, and aeroelastic deflections are based on deformations of this box. The box is described as a thin walled beam with vertical fore and aft spars and parabolic upper and lower surfaces.

For verification studies, the general box shape given in figure 6 was used, scaled in the vertical axis to match t/c. Maximum thickness was set near 35% chord; fore and aft spar locations and heights varied between aircraft. The resulting cross section provided a reasonable representation of actual aircraft structural box geometry.

Figure 6: Model Structural Cross Section.

The structural box is sized in spanwise sections. Each section has uniform wall thickness over its cross section. This thickness is set by either maximum bending stress or smeared minimum gauge. The structural

analysis evaluates wing loads at several potentially critical conditions, including maneuver and vertical gust. The largest bending moments experienced are used for structural sizing. These moments are multiplied by 1.5 to account for the ultimate load specified in FAR part 25. Section wall thicknesses are set so that maximum stresses on each cross section do not exceed an allowable stress, which is a fraction of the material yield stress. Properties of 2024-T4 aluminum are used as given by [3]: $E = 72.4$ GPa (10.5×10^6 psi), $G = 27.6$ GPa (4.0×10^6 psi), $\sigma_y = 331$ MPa (48×10^3 psi).

The allowable stress was set at 69% of yield stress. This factor was chosen to provide accurate total weight and wing stiffness predictions for a set of commercial aircraft wings. In concept, the 69% factor accounts for weight varying proportionally with the bending weight, but which is not explicitly calculated. In particular, the correction accounts for material to resist shear and fatigue.

The material outside the structural box is assumed to be at smeared minimum gauge. This is described as a skin thickness but includes material such as ribs, stiffeners, joints, and fasteners. In the wing box, these items are smeared into the walls to simplify calculation of bending and torsional inertias. The minimum gauge used is not a true minimum gauge but indicates an average amount of material used for each unit of wetted area. The minimum gauge used, 6.35 mm (0.25 in), was selected from correlation with weights of test wings.

Within the structural box, sections are sized to the larger of the thickness required for bending strength or the minimum gauge thickness. This yields the box weight. Total wing weight is obtained by adding the area dependent minimum gauge weight of the structure outside the box.

While testing and calibrating the analysis, the code was improved to account for airfoil section pitching moment and inertial bending relief from weight of the wing, fuel, and any wing mounted engines.

Data from three different aircraft were used in the study. Models of the DC9-30, DC10-10, and B727-200 were created and analyzed. The actual wing geometries analyzed are plotted in figure 7. Specific data on the geometry and flight conditions used are listed below.

B727-200:

Model Data:

Span:	32.87 m (107.9 ft)
Area:	157.90 m² (1700 ft²)
Root chord:	8.58 m (28.1 ft)
Break chord (chord at 35% span):	5.14 m (16.9 ft)
Tip chord:	2.24 m (7.3 ft)
Sweep:	32°
Forward spar location:	0.16 chord
Aft spar location:	0.60 chord
Spanwise panels:	20

Structural Design Condition:

Weight:	824141 N (185267 lb)
Altitude:	6250 m
Mach number:	0.88
Gust velocity:	20.87 m/s (68.5 ft/s)

Half Wing Results:

	estimate	actual	ratio
wing weight	4241 kg	4202 kg	1.01
	9350 lb	9264 lb	
box weight	2669 kg		
	5884 lb		
fuel weight	7370 kg		
	16248 lb		

DC10-10:

Model Data:

Span:	47.22 m (154.9 ft)
Area:	358.70 m² (3861 ft²)
Root chord:	13.94 m (45.7 ft)
Break chord (chord at 40% span):	7.86 m (25.8 ft)
Tip chord:	2.86 m (9.4 ft)
Sweep:	35°
Forward spar location:	0.15 chord
Aft spar location:	0.65 chord
Engine mass:	5731 kg (12635 lb) at 32.5% span
Spanwise panels:	20

Structural Design Condition:

Weight:	1963300 N (441350 lb)
Altitude:	7620 m (25000 ft)
Mach number:	0.88
Gust velocity:	20.86 m/s (68.4 ft/s)

Half Wing Results:

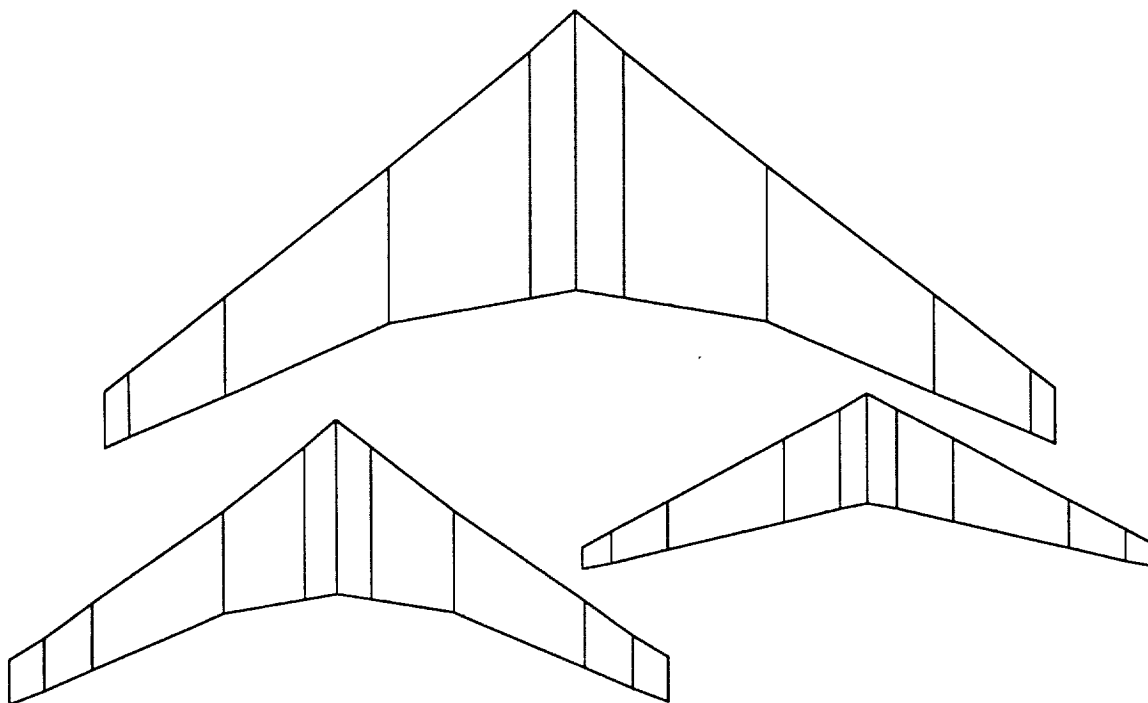|	estimate	actual	ratio
wing weight	11175 kg	11109 kg	1.01
	24637 lb	24491 lb	
box weight	7990 kg	7628 kg	1.05
	17615 lb	16817 lb	
fuel weight	29355 kg	33069 kg	
	64716 lb	72904 lb	

Figure 7: The planforms described in the following aircraft models are shown from left to right: B727, DC10, DC9.

DC9-30:

Model Data:

Span:	28.44 m (93.3 ft)
Area:	92.97 m² (1001 ft²)
Root chord:	5.43 m (17.8 ft)
Tip chord:	1.10 m (3.6 ft)
Sweep:	24.5°
Forward spar location:	0.15 chord
Aft spar location:	0.62 chord
Spanwise panels:	20

Structural Design Condition 1:

Weight:	465984 N (104753 lb)
Altitude:	7620 m (25000 ft)
Mach number:	0.83
Gust velocity:	20.86 m/s (68.4 ft/s)

Half Wing Results (Condition 1):

	estimate	actual	ratio
wing weight	2381 kg	2583 kg	0.92
	5249 lb	5695 lb	
box weight	1506 kg	1587 kg	0.95
	3320 lb	3499 lb	
fuel weight	3025 kg	4762 kg	
	6669 lb	10498 lb	

Structural Design Condition 2:

Weight:	522252 N (117402 lb)
Altitude:	7620 m (25000 ft)
Mach number:	0.80
Gust velocity:	20.86 m/s (68.4 ft/s)

Half Wing Results (Condition 2):

	estimate	actual	ratio
wing weight	2617 kg	2583 kg	1.01
	5769 lb	5695 lb	
box weight	1742 kg	1587 kg	1.10
	3840 lb	3499 lb	
fuel weight	3025 kg	4762 kg	
	6669 lb	10498 lb	

Deflection Calculation Condition:

Weight:	465984 N (104753 lb)
Altitude:	9145 m (30000 ft)
Mach number:	0.75
Wing structure:	same as condition 2 above.

Total weight estimates are quite good for the DC10 and B727. The DC9 total weight estimate varies depending on the assumed aircraft weight. The first assumed design condition is based on the original DC9-30 maximum takeoff weight while the second design condition is based on the DC9-34 maximum takeoff weight. Since DC9-30 and DC9-34 wings are essentially the same, there is some question as to whether
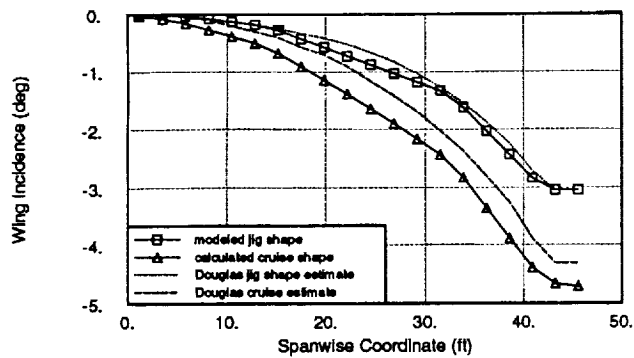
Figure 8: Incidence Distributions for DC9. Calculated incidences are compared with Douglas estimates to check the accuracy of aeroelastic calculation.

the DC9-30 wing was designed initially with aircraft growth in mind. The following line from Francillon, [4], suggests this to be the case.

> From the onset of the DC-9 programme, the aircraft had been planned for substantial growth as its MGTOW was initially limited to less than 80,000 lb to fit within the then current FAA restrictions for operations by a two-man crew whilst it had to use JT8D turbofans derated from their normal take-off thrust of 14,000 lb (6,350 kg) to 12,000 lb (5,443 kg).

The analysis gets close results when the DC9-34 aircraft weight is used.

The method slightly overpredicts wing box weight for the DC10 and DC9 (with DC9-34 aircraft weight). This is of less concern than getting accurate total wing weight and deflections. Wing deflections are indicated by the elastic wing incidence distributions plotted in figure 8. For comparison, figure 8 also provides incidence distributions estimated by Douglas, [5]. The deflection calculation is quite good with only a 0.4° difference in twist at the tip. This difference occurs partly because stiffening of the wing root due to the fuselage is not modeled. The simplification of considering only the wing box in calculating elastic deformations also misses some stiffness contributed by material in the leading edge and trailing control surfaces. The result is a slight underprediction in wing stiffness. The overprediction of box weight increases the amount of load carrying material to improve the prediction of wing stiffness.

Maximum Lift

An accurate prediction of maximum lift is a prerequisite to selection and optimization of wing area. In order to free wing area as an optimization variable,

work was done to improve the maximum lift analysis, particularly for predicting lift in the flaps down condition.

A method for predicting section $c_{l_{max}}$ with flaps down was implemented in the code and a method was developed for making corrections to $c_{l_{max}}$ due to induced camber at the flap edge. The maximum lift analysis was verified against flight test data from DC9 and DC10 aircraft.

Basic Approach

A critical section approach is used for predicting wing $C_{L_{max}}$. The distribution of section c_l is calculated and is compared with the local $c_{l_{max}}$ at each spanwise section. The wing is said to be at $C_{L_{max}}$ when the lift coefficient on any section reaches local $c_{l_{max}}$.

This method gives surprisingly good results, possibly for the following reason: commercial transport wings must be designed to provide good handling qualities at stall. This means that stall should never begin at the wing tips since an asymmetric stall could cause the aircraft to roll out of control. In practice, because of aft sweep, a conventional transport wing is prone to stall at the wing tips, and aircraft designers modify airfoil sections on the inboard sections to degrade the $c_{l_{max}}$ of those sections and ensure stall beginning at the wing root. The wing is designed to stall at, or just below, the point where the critical section reaches its $c_{l_{max}}$.

The specific procedure used compares the streamwise c_l calculated from the 3D Weissinger model with the 2D $c_{l_{max}}$ of the streamwise section. No conversion is made to sections perpendicular to the wing sweep axis. This is still a topic under study, but the assumption made during this work was that the viscous boundary layer flow follows the streamwise direction more closely than the sweep perpendicular direction, making a comparison between streamwise c_l and $c_{l_{max}}$ a better indicator of stall than a comparison in the sweep perpendicular direction.

To simulate a wing with flaps deployed, 2D section data is again employed. In 2D, flap deflection increases the c_l at zero angle of attack and increases $c_{l_{max}}$. We note these changes with Δc_l and $\Delta c_{l_{max}}$ respectively.

$$\Delta c_l = \Delta c_l(\delta)$$

$$\Delta c_{l_{max}} = \Delta c_{l_{max}}(\delta)$$

Δc_l and $\Delta c_{l_{max}}$ are functions of δ and partially reflect viscous effects. In translating this to 3D, incidences on the Weissinger model are incremented an amount, $\Delta \alpha$, that gives a lift increment equivalent to that generated by the flap.

$$\Delta \alpha = \frac{\Delta c_l}{c_{l_\alpha}}$$

8

This $\Delta\alpha$ is applied to the streamwise airfoil section and the Weissinger model automatically handles effects due to sweep. Calculation of section stall is done as with unflapped sections except that $\Delta c_{l_{max}}$ is added to the section $c_{l_{max}}$.

When this approach is used to calculate $C_{L_{max}}$ for a wing with flaps deployed, a problem occurs. The critical section appears adjacent to the flapped portion of the wing, on the unflapped portion. The flap induces upwash on this section, increasing section lift. This upwash has a chordwise variation that alters the effective camber of the sections adjacent to the flap. The change in effective camber should increase the section $c_{l_{max}}$, but in the standard critical section analysis, the $c_{l_{max}}$ of the geometric section is used without correction for induced camber. The load calculation captures the extra c_l due to flap upwash, but when compared with uncorrected section $c_{l_{max}}$, stall is predicted prematurely. The simple critical section approach underpredicts $C_{L_{max}}$ of wings with flaps deployed.

Induced Camber Estimation

To correct for this problem, a rational method for estimating the induced camber is desired. From this, adjustments to the $c_{l_{max}}$ distribution could be made to yield more accurate predictions of wing $C_{L_{max}}$.

The first step toward developing a method for estimating the induced effects is to identify the primary source of the induced velocities as the shed vorticity concentrated around the flap edge. Induced velocities are proportional to the total shed vorticity, which is proportional to the extra vorticity carried on the flapped section. Induced angles are proportional to the shed vorticity divided by the U_∞. Recalling $c_l = \frac{2\Gamma}{U_\infty c}$, the induced angles are proportional to the extra c_l carried on the flapped section.

The shed vorticity at the flap edge is actually distributed so the lift distribution is continuous and there are no infinite induced velocities. Despite this, the shed vorticity is sufficiently concentrated that the induced velocities may be approximated by a radially symmetric spatial relation, as would be the case for a true vortex.

From these observations, a function for estimating an induced flap deflection can be proposed.

$$\delta_i = \frac{\Delta c_{l_g}}{2c_{l_\delta}} \left[\frac{1}{1 + c_h(\frac{h}{c}) + c_{xx}(\frac{x}{c})^2 + c_{hh}(\frac{h}{c})^2} \right] \hat{\theta} \cdot \hat{n}$$

Here Δc_{l_g} is the increment in 2D section c_l due to geometric flap deflection. It indicates the strength of the vorticity trailing from the flap edge. c_{l_δ} is the 2D flap lift curve slope. It properly converts c_l to flap deflection. The coefficients, c_h, c_{xx}, and c_{hh} are fit constants

to be determined by comparison with test calculations of δ_i for representative geometries. x and h are spatial factors. They are components of a position vector between three-quarter chord points of the flap edge section and any section. x gives the distance in the $\hat{x}$ direction; h gives the distance perpendicular to the $\hat{x}$ direction: $h = \sqrt{y^2 + z^2}$. The dot product, $\hat{\theta} \cdot \hat{n}$, gives δ_i the correct sign according to the direction of induced velocity, $\hat{\theta}$ and the local panel normal, $\hat{n}$. The induced flap angle changes from negative to positive when moving from the flapped to unflapped wing sections.

A set of Lin Air models were used to obtain estimates of δ_i. The models had very large aspect ratios to simulate "infinite" wings. Different sweep angles were used to determine sweep effects. Two chordwise panels were used, simulating the main wing section and a 25% chord flap. This configuration is fairly representative of commercial transport wings.

For this paneling, in 2D, velocities induced at the control points by the vortices are

$$v_1 = \frac{1}{2\pi c} \left[\tfrac{8}{3}\Gamma_1 - 4\Gamma_2 \right]$$

$$v_2 = \frac{1}{2\pi c} \left[\tfrac{4}{3}\Gamma_1 + 8\Gamma_2 \right]$$

Induced velocities are equated to free stream velocities through the control points, enforcing tangent flow boundary conditions.

$$v_1 = \alpha\, U_\infty$$

$$v_2 = (\alpha + \delta)\, U_\infty$$

This yields a set of equations to be solved for Γ_1 and Γ_2.

$$\frac{1}{2\pi c} \begin{bmatrix} \tfrac{8}{3} & -4 \\ \tfrac{4}{3} & 8 \end{bmatrix} \begin{Bmatrix} \Gamma_1 \\ \Gamma_2 \end{Bmatrix} = \begin{Bmatrix} \alpha \\ \alpha + \delta \end{Bmatrix} U_\infty$$

$$\frac{\Gamma_1}{U_\infty} = \frac{2\pi c(12\alpha + 4\delta)}{80/3}, \quad \text{and} \quad \frac{\Gamma_2}{U_\infty} = \frac{2\pi c(\tfrac{4}{3}\alpha + \tfrac{8}{3}\delta)}{80/3}$$

Before proceeding further, the problem should be translated to 3D. Since, for now, we are dealing only in inviscid flow, simple sweep theory holds. The following transformations apply:

$$c \rightarrow c \cos \Lambda$$

$$U_\infty \rightarrow U_\infty \cos \Lambda$$

$$\alpha \rightarrow \frac{\alpha}{\cos \Lambda}$$

$$\delta \rightarrow \frac{\delta}{\cos \Lambda}$$

When applied to the equation for Γ_1 and Γ_2, the net change is that the chord length is replaced by $c \cos \Lambda$.

$$\frac{1}{2\pi c \cos \Lambda} \begin{bmatrix} \tfrac{8}{3} & -4 \\ \tfrac{4}{3} & 8 \end{bmatrix} \begin{Bmatrix} \Gamma_1 \\ \Gamma_2 \end{Bmatrix} = \begin{Bmatrix} \alpha \\ \alpha + \delta \end{Bmatrix} U_\infty$$

9

The solution for section Γ_1 and Γ_2 in 3D is

$$\frac{\Gamma_1}{U_\infty} = \frac{2\pi c \cos \Lambda(12\alpha + 4\delta)}{80/3}$$

$$\frac{\Gamma_2}{U_\infty} = \frac{2\pi c \cos \Lambda(\frac{4}{3}\alpha + \frac{8}{3}\delta)}{80/3}$$

where α and δ are referenced to the streamwise section.

Lift coefficients of the panels can be evaluated using

$$c_l = \frac{2\Gamma}{U_\infty c}$$

From this we obtain

$$c_{l_1} = \frac{2\pi \cos \Lambda}{3/4} \left(\tfrac{9}{10}\alpha + \tfrac{3}{10}\delta\right)$$

$$c_{l_2} = \frac{2\pi \cos \Lambda}{1/4} \left(\tfrac{1}{10}\alpha + \tfrac{1}{5}\delta\right)$$

The Lin Air analysis provides values of c_{l_1} and c_{l_2} from which effective α and δ may be backed out using the above equations.

$$\alpha = \frac{2c_{l_1} - c_{l_2}}{4\pi \cos \Lambda}$$

$$\delta = \frac{3c_{l_2} - c_{l_1}}{4\pi \cos \Lambda}$$

The effective flap deflection, δ, is composed of parts due to geometry, δ_g, and induced velocities, δ_i.

$$\delta = \delta_g + \delta_i$$

By subtracting δ_g from the δ calculated from Lin Air, the induced δ_i can be obtained.

Three wings were modeled in Lin Air to get estimates of effective δ. Sweep on these wings, shown in figure 9, varied from $0°$, to $20°$, to $40°$. The spatial fit coefficients, c_h, c_{xx}, and c_{hh}, were selected to give close estimates of δ_i, giving the following results.

$$c_h = 13, \quad c_{xx} = 151, \quad c_{hh} = 18$$

In figures 10 through 12, estimates of δ from the spatial fit are compared with calculated values from Lin Air. The spatial fit does a good job at matching the data in these examples.

To justify the use of this quasi-empirical estimate for δ_i it must be applied to a realistic configuration. Lin Air was again used to get data on effective δ, but on a simulated DC9 planform. This model introduced spanwise variation in chord and 36% chord flaps as opposed to the 25% chord flaps used in the previous models.

Variation in chord is expected to affect δ_i somewhat. However the induced velocities that cause δ_i diminish very quickly on either side of the flap edge. Over the
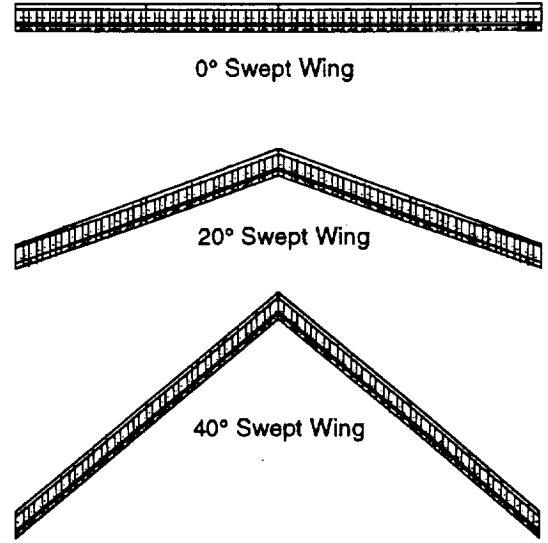

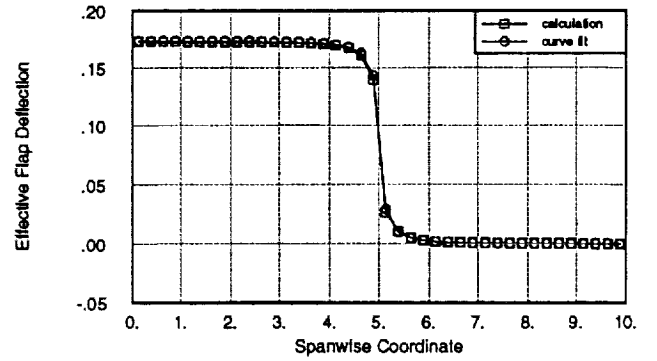Figure 9: Model Planforms for Determining Induced Flap Deflection.

Figure 10: Effective Flap Deflections on $0°$ Swept Wing. Incidences calculated with Lin Air are compared with estimates generated using the proposed fit to δ_i.
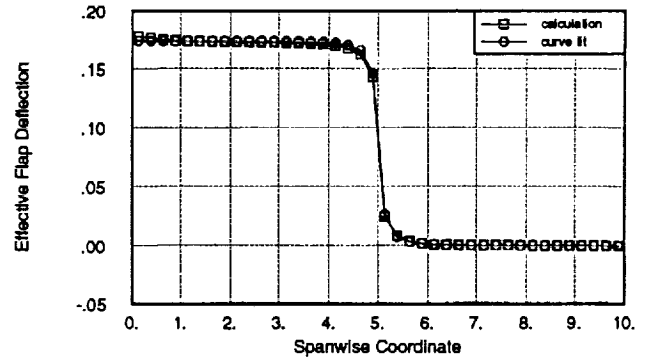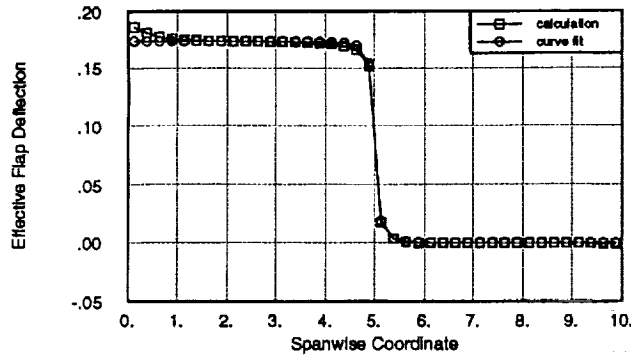

Figure 11: Effective Flap Deflections on $20°$ Swept Wing. Incidences calculated with Lin Air are compared with estimates generated using the proposed fit to δ_i.

10

Figure 12: Effective Flap Deflections on 40° Swept Wing. Incidences calculated with Lin Air are compared with estimates generated using the proposed fit to δ_i.
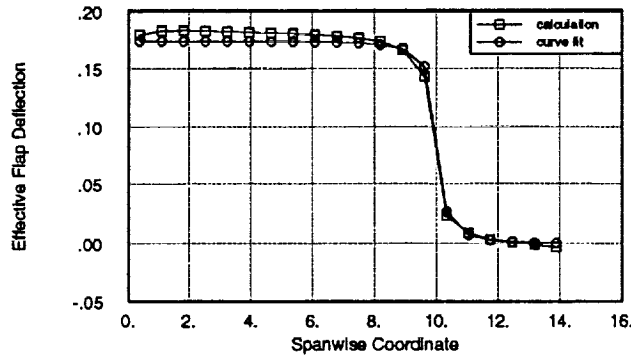

Figure 13: Effective Flap Deflections on Simulated DC9 Wing. Incidences calculated with Lin Air are compared with estimates generated using the proposed fit to δ_i.
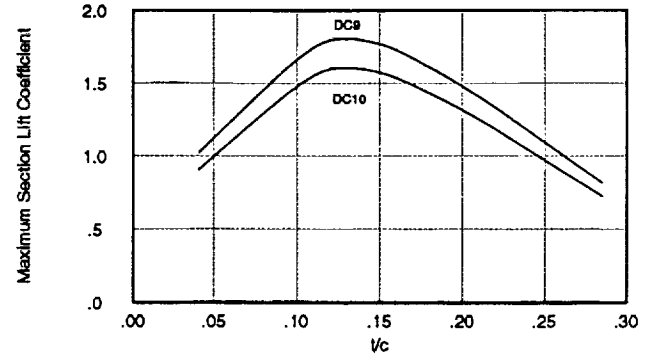

Figure 14: Model for maximum section lift coefficient as a function of t/c. The curves are estimates to $c_{l_{max}}$ for families of airfoils based on the DC9 and DC10 sections.
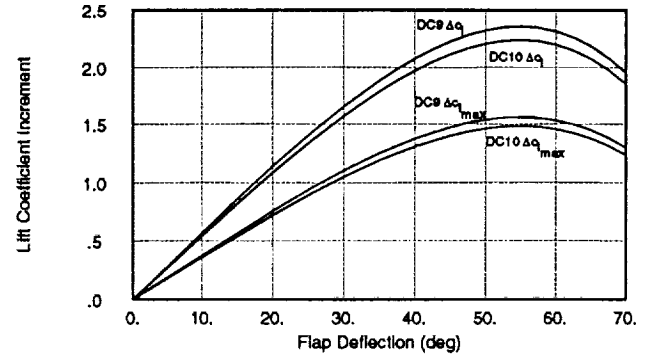

Figure 15: Model for the increment in section lift due to flap deflection, Δc_l, and the increment in maximum section lift, $\Delta c_{l_{max}}$. The difference between the curves is due to different flap chord to wing chord ratios: 36% on DC9, 32% on DC10.

local region where the induced velocities are important, the variation in chord is usually small, enabling effects of taper to be neglected.

The change in flap chord affects the calculation of δ from Lin Air. The paneling in this case is the same as before, except that the main element uses the first 64% chord and the flap element uses the last 36% chord. This changes the equations for v_1 and v_2, and the subsequent steps can be repeated to get the following equation for δ.

$$\delta = 1.14\overline{6}\frac{3c_{l_2} - c_{l_1}}{4\pi\cos\Lambda}$$

c_{l_δ} also differs from the result for 25% chord flap.

$$c_{l_\delta} = 1.255813951\pi$$

When the above modification to the 2D section analysis are used with the spatial fit to δ_i developed earlier, a good estimate of effective δ can be achieved as shown in figure 13.

Comparison with Flight Test

The final test of the method for estimating induced flap incidence was to use the formula for δ_i within the wing optimization program and attempt to match flight test data for the DC9 and DC10. Empirical data were used for $c_{l_{max}}$, Δc_l, and $\Delta c_{l_{max}}$. Basic section $c_{l_{max}}$ was estimated from data provided in [6] and [7]. Increments to section lift, Δc_l and $\Delta c_{l_{max}}$, were estimated using methods suggested by [8]. The models are described in figures 14 and 15. The resulting aircraft $C_{L_{max}}$ is plotted as a function of flap deflection in figure 16, where flight test data from [9] is also provided for comparison.

Application of Method

With the modifications to the analysis methods listed above, the optimization program was used for a study exploring the effect of design for laminar flow on a business jet. This study was done to assist work in a cooperative agreement between NASA and Learjet.
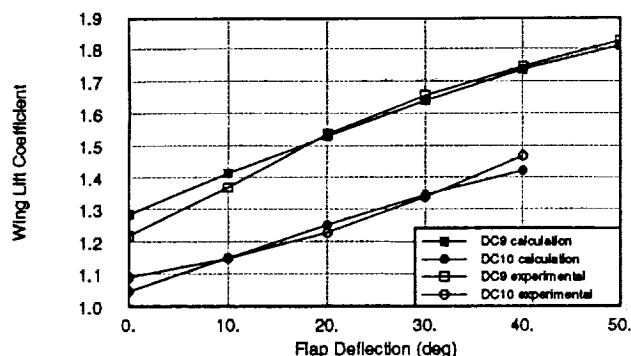
11

Figure 16: Maximum lift calculated by the wing optimization program using the δ_i correction are compared to flight test data. The variation with flap deflection is shown for DC9 and DC10 aircraft. Configurations examined are with slats retracted.

In the study, wings were optimized for minimum cruise drag subject to fixed weight and minimum safe speed constraints. The specific design conditions are listed below.

Cruise Design Condition:

Weight:	73371 N (16494 lb)
Altitude:	10668 m (35000 ft)
Mach number:	0.82

Structural Design Condition:

Weight:	73371 N (16494 lb)
Altitude:	7620 m (25000 ft)
Mach number:	0.88
Maneuver load factor:	2.5
Gust velocity:	20.0 m/s (65.6 ft/s)

Minimum Speed Requirements:

Clean:	73.7 m/s (143 kt)
Flaps down:	64.5 m/s (125 kt)

The aircraft is expected to be designed for a cruise Mach number of 0.85; however the compressibility drag routines implemented in the code are for old peaky airfoil sections and it is expected that supercritical airfoil sections will reduce divergence Mach number by 0.03. This explains the choice of 0.82 cruise Mach number for the study.

To simulate effects of laminar flow, the value of skin friction coefficient was reduced in the parasite drag model. Skin friction coefficient was reduced 20% as an estimate for a 40% run of laminar flow. In exchange for skin friction reduction, wings designed for laminar flow were given sweep constraints. These constraints represent difficulties in achieving laminar flow at high sweep angles because of cross flow instability. Laminar flow is assumed only on the outer wing elements. Turbulent flow, and its higher c_f, are assumed on the inboard wing elements. Laminar flow is not expected on the inboard elements because of contamination from the fuselage boundary layer. To minimize any loss from

this, no constraint is placed on inboard section sweep. To obtain laminar flow on the outboard wing panels, it is expected that a boundary layer fence will be placed between the turbulent inboard and laminar outboard sections.

The results of the study are shown in figure 17 and table 4. This study was the first to use the method with wing area as a design variable. The previously mentioned improvements to structural and maximum lift analyses were crucial to making proper optimizations of wing area, and the results of this study suggest the necessity of such optimization.

The laminar flow designs have more wing area than their conventional counterparts. Designs D, E, and F have 8%, 16%, and 17% more area than designs A, B, and C, respectively. Compared with the turbulent flow designs of similar weight, the laminar flow wings have less parasite drag, and more compressibility drag because of the sweep constraint. Since the cost of adding wing area is small for laminar flow wings, the optimizer increases wing area to reduce c_l and hence compressibility drag. Had this been a fixed area study and the laminar flow wings were forced to have the same area as the conventional ones, the laminar flow design strategy would have been unfairly disadvantaged, stuck with less than optimal wing area.

One fixed parameter that may have an important effect on this study is cruise altitude. A fixed altitude constraint is reasonable to assume as it is either set by operational considerations or by engine performance. Comparing the drag of wings at different altitudes is of limited utility since engine performance is very sensitive to altitude. The 35000 ft cruise altitude used in this study may be on the low end for desired business jet operations, but it probably serves as a good altitude to compare laminar and turbulent flow designs. As wing weight increases, designs presumably move toward aerodynamic optimums: the area on turbulent flow wings decreases, indicating minimum drag at higher C_L; the area on laminar flow wings increases, indicating minimum drag at lower C_L. The performance of laminar flow wings relative to conventional wings will likely improve at lower altitude and diminish at higher altitude.

The study was done initially with a 20° constraint on wing sweep for laminar flow. This was perceived as a sweep angle which could be reasonably expected to give laminar flow, but as indicated in figure 17, laminar flow design provides no advantage over conventional design with this sweep constraint. Indicated in table 4, the sweep constraint creates a large compressibility drag penalty, more than three times the compressibility drag on turbulent flow wings of similar weight. Wing area is increased to compensate, but this reduces structural efficiency, leading to shorter spans and higher induced

12

| | Turbulent Flow Cases | | | Laminar Flow Cases | | | | | |
	Design A:	Design B:	Design C:	Design D:	Design E:	Design F:	Design G:	Design H:	Design I:
BaseSemiArea	9.86	9.79	9.75	10.65	11.31	11.42	9.96	9.97	9.98
BaseSemiSpan	5.68	6.41	6.98	5.24	5.72	6.26	5.62	6.36	7.00
AreaFracA	0.388	0.388	0.388	0.387	0.388	0.389	0.388	0.389	0.389
AreaFracB	0.331	0.332	0.332	0.331	0.332	0.332	0.329	0.331	0.331
TaperA	0.837	0.841	0.833	0.870	0.888	0.892	0.838	0.920	0.909
SweepA	37.1	37.4	37.6	36.1	36.8	36.9	36.7	37.2	37.4
IncR1	0.63	0.46	0.28	1.74	1.32	1.33	1.10	1.14	0.98
IncT2	0.51	0.10	-0.33	-2.70	-1.63	-1.76	-1.24	-0.97	-1.34
IncT3	-1.88	-1.45	-0.92	-4.21	-3.00	-2.93	-2.47	-2.73	-2.23
IncT4	-4.25	-3.66	-3.13	-4.59	-3.32	-3.12	-4.37	-3.33	-2.85
TonCR1	0.138	0.135	0.133	0.140	0.137	0.136	0.138	0.130	0.129
TonCT2	0.112	0.114	0.115	0.096	0.088	0.087	0.109	0.106	0.106
TonCT3	0.117	0.117	0.115	0.095	0.090	0.089	0.109	0.110	0.109
TonCT4	0.127	0.125	0.123	0.112	0.103	0.102	0.135	0.127	0.125
ftot	0.332	0.306	0.290	0.374	0.337	0.318	0.313	0.287	0.270
finv	0.114	0.091	0.076	0.136	0.110	0.093	0.114	0.092	0.076
fvis	0.207	0.206	0.205	0.186	0.194	0.195	0.177	0.176	0.176
fcpr	0.010	0.010	0.009	0.053	0.033	0.030	0.022	0.018	0.017

Table 4: Comparison of Laminar and Turbulent Flow Wing Designs. Optimized results for all design variables are shown. The geometry description is similar to that used for the study in the Optimizer Directed Structural Sizing subsection. The element layout is the same described in figure 3, except only four sub elements are used: element A contains both sub elements 1 and 2, elements B and C contain sub elements 3 and 4 respectively. BaseSemiSpan is the wing semi span in meters. BaseSemiArea is the wing semi area in square meters. AreaFracA and AreaFracB are the fractions of total wing semi area allocated to elements A and B. AreaFracC is implicitly allocated any remaining wing area. TaperA is the taper ratios of element A. TaperB and TaperC are determined from continuity of chord between elements. SweepA is the wing quarter chord sweep for turbulent flow designs (A to C); it is the inboard section sweep for laminar flow designs (D to I). Inc and TonC are incidence and thickness to chord ratio values for the sub elements. Location on the sub element is given by the suffixed R or T: R for root, T for tip. Final digit suffix indicates which sub element. Values not given in the table are defined by linearly interpolating between given values. Equivalent drag areas are given so designs may be compared on particular drag components. The posted values, ftot, finv, fvis, and fcpr, correspond to total, induced, parasite, and compressibility drag areas in square meters.

drag.

The sensitivity of drag with wing sweep was estimated for laminar flow wings by optimizing with a 30° sweep constraint. A reduction in drag relative to conventional designs is indicated in figure 17. It is not clear whether substantial amounts of laminar flow can be achieved on a 30° swept wing. Interpolating between designs C, F, and I, it appears that laminar flow must be demonstrated on wings with at least 26° sweep before laminar flow design becomes useful for this particular mission.
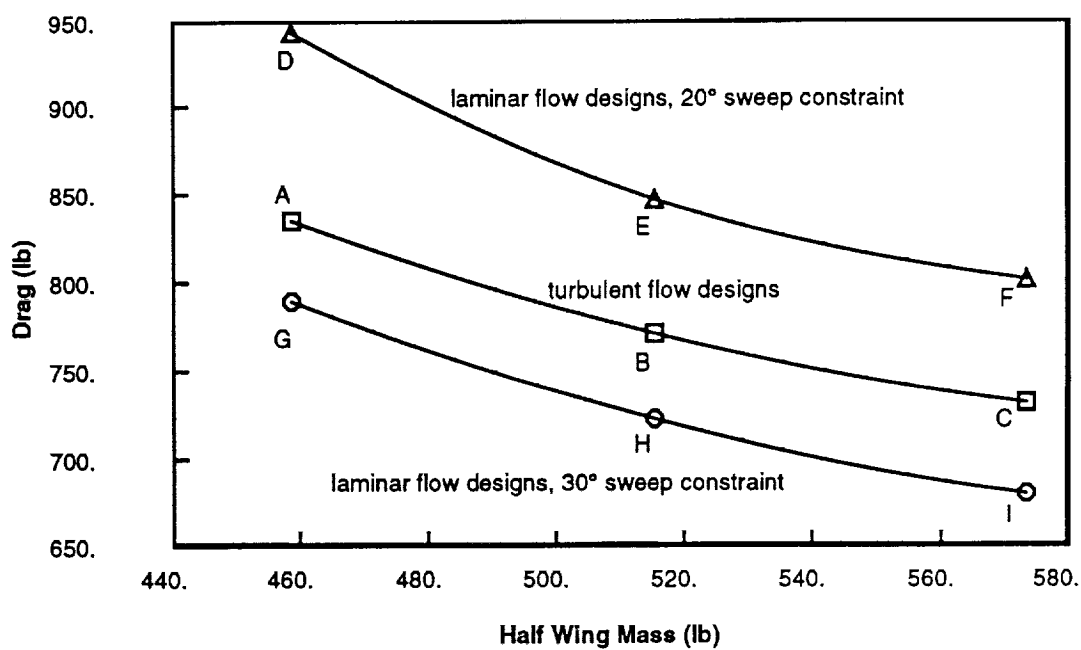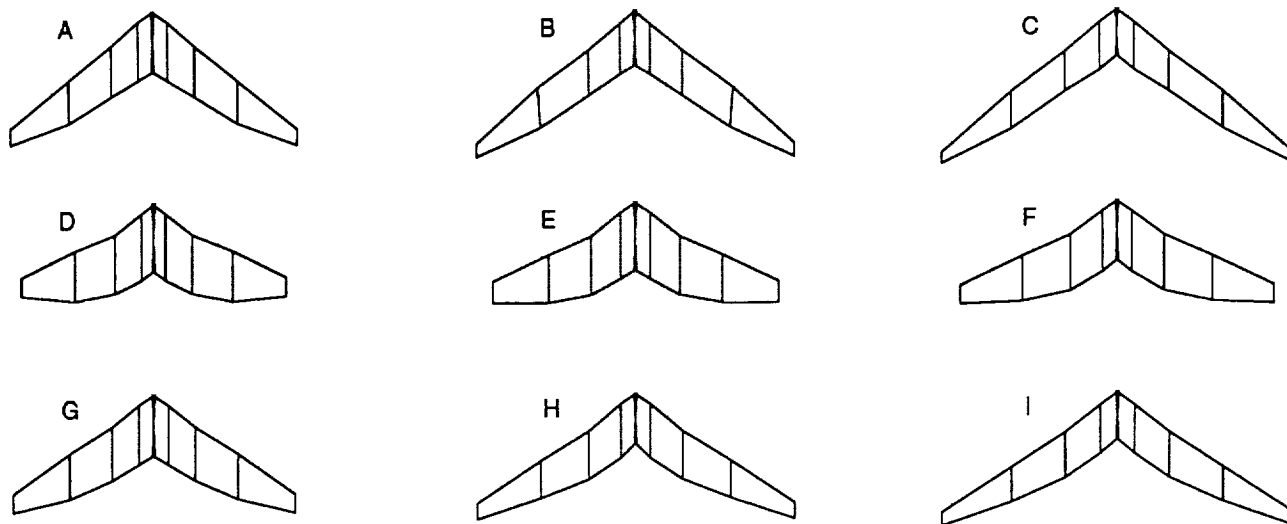
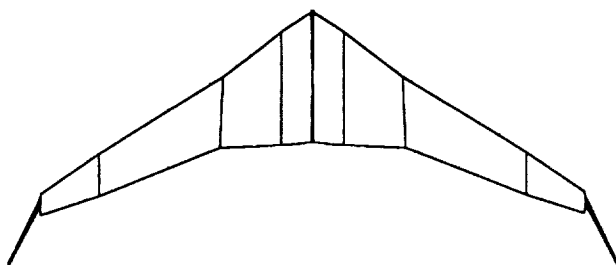Figure 17: Comparison of Laminar and Turbulent Flow Wing Designs.

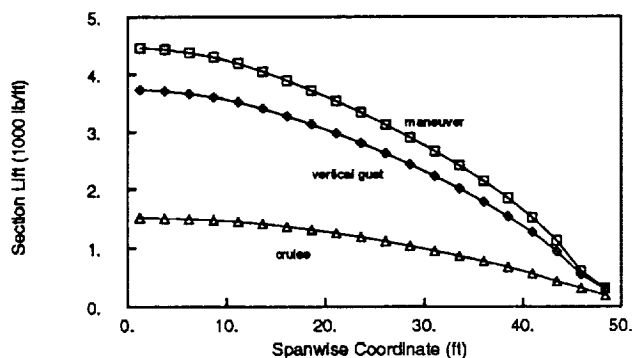**Figure 18: Optimized Planform with Wingtip Sweep as a Design Variable.**

Figure 19: Section Lift Distributions on Optimized Wingtip Sweep Planform.

Figure 20: Section Lift Coefficient Distributions on Optimized Wingtip Sweep Planform.

Current Status

As a first step toward making comparisons of different wing tip devices, an optimization was run with sweep of the tip element as a design variable. The resulting wing, and its distributions of lift and c_l are plotted in figures 18 through 20. The wing tip is planar with a sweep of 54°. The high sweep means the tips have no compressibility drag and can have high lift coefficients in cruise. Since lift curve slope varies like $\cos \Lambda$, the wing tips load more slowly with angle of attack than the main wing. This gives section c_l's comparable to the main wing at low speed, and leaves the tips relatively unloaded in the structural sizing load case. The optimizer found several advantages to sweeping the wing tips.

While the direction for improvement is good, the extent taken in this example is not correct because of effects not modeled in the analysis methods. The most obvious is that section $c_{l_{max}}$ has not been adjusted for sweep.

This is not simply an oversight; there does not seem to be a definitive method for handling sweep effects on maximum lift. While some references take $c_{l_{max}}$ as varying like $\cos \Lambda$, [8], experiments suggest that higher values of $c_{l_{max}}$, approaching those of unswept wings, can be achieved, [10, 11].
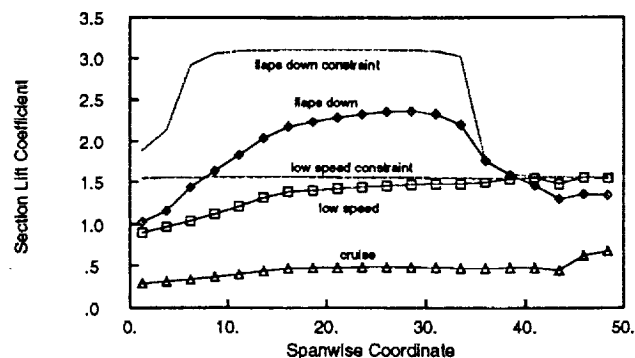
Additional work on $C_{L_{max}}$ prediction is expected as this work continues. The current goal is to find or develop a method that accurately predicts the effects of sweep on section $c_{l_{max}}$. Additional work on the structural model is also expected, primarily on implementing an estimate for shear material, which may be important in the analysis of swept wingtips and business jet wings. When these further analysis modifications are finished, it is hoped that practical studies of wingtip devices and optimal planform shapes can be made.

References

[1] Smith, S. C., and Kroo, I. M., "A Closer Look at the Induced Drag of Crescent-Shaped Wings," AIAA-90-3063, 1990.

[2] Wakayama, S., and Kroo, I., "A Method for Lifting Surface Design Using Nonlinear Optimization," AIAA-90-3290, 1990.

[3] Miner, D. F., and Seastone, J. B., Eds., *Handbook of Engineering Materials*, 1st Ed., John Wiley & Sons Inc., 1955.

[4] Francillon, Rene J., *McDonnell Douglas Aircraft since 1920*, Vol. 1, Naval Institute Press, Annapolis, Maryland, 1988.

[5] "Estimated Aerodynamic Data for Stability and Control Calculations Model DC-9-30 Transport", Douglas Aircraft Company Report LB-32322, 1967.

[6] Abbot, I., and Van Doenhoff, A., *Theory of Wing Sections*, Dover Publications, New York, 1959.

[7] Shevell, R. S., Private Communication, Department of Aeronautics and Astronautics, Stanford University.

[8] Torenbeek, E., *Synthesis of Subsonic Airplane Design*, Delft University Press, Delft, Holland, 1982.

[9] Shevell, R. S., *Fundamentals of Flight*, 2nd Ed., Prentice Hall, New Jersey, 1989.

[10] Furlong, G. Chester, and McHugh, James G., "A Summary and Analysis of the Low Speed Longitudinal Characteristics of Swept Wings at High Reynolds Number," NACA Report 1339, 1957.

[11] Letko, William, and Goodman, Alex, "Preliminary Wind Tunnel Investigation at Low Speed of Stability and Control Characteristics of Swept Back Wings," NACA TN 1046, 1946.